frontiers | Frontiers in Energy Research

TYPE Original Research
PUBLISHED 02 December 2022
DOI 10.3389/fenrg.2022.983979

OPEN ACCESS

EDITED BY
Juliusz Dąbrowa,
AGH University of Science and Technology, Poland

REVIEWED BY
Aleksey Yaremchenko,
University of Aveiro, Portugal
Yinlong Zhu,
Monash University, Australia

*CORRESPONDENCE
Simon Schweidler,
simon.schweidler@kit.edu
Miriam Botros,
miriam.botros@kit.edu

SPECIALTY SECTION
This article was submitted to Electrochemical Energy Conversion and Storage, a section of the journal Frontiers in Energy Research

RECEIVED 01 July 2022
ACCEPTED 23 November 2022
PUBLISHED 02 December 2022

CITATION
Schweidler S, Tang Y, Lin L, Karkera G, Alsawaf A, Bernadet L, Breitung B, Hahn H, Fichtner M, Tarancón A and Botros M (2022), Synthesis of perovskite-type high-entropy oxides as potential candidates for oxygen evolution.
Front. Energy Res. 10:983979.
doi: 10.3389/fenrg.2022.983979

Synthesis of perovskite-type high-entropy oxides as potential candidates for oxygen evolution

Simon Schweidler[1]*, Yushu Tang[1], Ling Lin[1], Guruprakash Karkera[2], Alaa Alsawaf[1], Lucile Bernadet[3], Ben Breitung[1], Horst Hahn[1,4], Maximilian Fichtner[1,2], Albert Tarancón[3,5] and Miriam Botros[1]*

[1]Institute of Nanotechnology, Karlsruhe Institute of Technology (KIT), Karlsruhe, Germany, [2]Helmholtz Institute Ulm (HIU), for Electrochemical Energy Storage, Ulm, Germany, [3]Department of Advanced Materials for Energy, Catalonia Institute for Energy Research-IREC, Barcelona, Spain, [4]KIT-TUD Joint Research Laboratory Nanomaterials Institute of Materials Science, Technische Universität Darmstadt (TUD), Darmstadt, Germany, [5]Catalan Institution for Research and Advanced Studies (ICREA), Barcelona, Spain

High-entropy materials offer a wide range of possibilities for synthesizing new functional ceramics for different applications. Many synthesis methods have been explored to achieve a single-phase structure incorporating several different elements, yet a comparison between the synthesis methods is crucial to identify the new dimension such complex ceramics bring to material properties. As known for ceramic materials, the synthesis procedure usually has a significant influence on powder morphology, elemental distribution, particle size and powder processability. Properties that need to be tailored according to specific applications. Therefore, in this study perovskite-type high-entropy materials $(Gd_{0.2}La_{0.2-x}Sr_xNd_{0.2}Sm_{0.2}Y_{0.2})(Co_{0.2}Cr_{0.2}Fe_{0.2}Mn_{0.2}Ni_{0.2})O_3$ (x = 0 and x = 0.2) are synthesized for the first time using mechanochemical synthesis and a modified Pechini method. The comparison of different syntheses allows, not only tailoring of the constituent elements of high-entropy materials, but also to optimize the synthesis method as needed to overcome limitations of conventional ceramics. To exploit the novel materials for a variety of energy applications, their catalytic activity for oxygen evolution reaction was characterized. This paves the way for their integration into, e.g., regenerative fuel cells and metal air batteries.

KEYWORDS

high-entropy materials, oxygen evolution reaction (OER), perovskite-type oxide, catalysis, water splitting, energy storage and conversion

1 Introduction

The synthesis of novel materials is the first and most crucial step when designing materials for a specific application. A synthesis method that is not tailored to achieve certain material properties might overshadow even extraordinary intrinsic material properties. Such properties are currently expected of high-entropy materials, that

crystallize in a single-phase structure due to the increase of configurational entropy. High-entropy ceramics have been utilized as thermal barrier layers, catalysts and electrode materials for energy storage and conversion (Wang et al., 2019; Sarkar et al., 2020; Wang et al., 2020; Ma et al., 2021). The first synthesis methods to produce $(Co_{0.2}Cu_{0.2}Mg_{0.2}Ni_{0.2}Zn_{0.2})O$ rock salt-type high-entropy ceramics were solid state synthesis and nebulized spray pyrolysis (Rost et al., 2015; Sarkar et al., 2017a). Both result in single-phase materials with different powder morphologies which may lead to different yet unexplored properties. Another possible synthesis method that has been used to successfully produce materials with high entropy, such as oxides or oxyfluorides, without additional thermal treatment is mechanochemical synthesis (Lin et al., 2020). The synthesis method allows the incorporation of elements oxidized at high temperatures, like $Mn^{2+/3+}$, $Cr^{2+/3+}$, and $Fe^{2+/3+}$. In order to counteract an undesired oxidation of an element it is important to consider a charge compensation mechanism during synthesis e.g., by Li^+ incorporation, otherwise secondary phases are likely to form (Wang et al., 2020). For high-entropy materials the synergetic effect between the different elements is the key to achieving the desired performance (Ma et al., 2021). Nevertheless, the optimal performance can be impeded by other factors like particle size, agglomeration and thermal stability (Dąbrowa et al., 2020). Therefore, it is critical to identify the influence of the synthesis method on such novel, complex ceramics, decoupling the impact of the elemental composition from material processing. Synthesizing high-entropy perovskite-type ceramics using sol-gel method, for instance, was recently performed aiming for optimal properties for the application as an air-electrode in solid oxide fuel cells (SOFC) (Dąbrowa et al., 2020). Perovskites (ABO_3) are considered very promising candidates as catalysts for oxygen evolution reaction (OER) opening new possibilities for cost-effective catalysts with applications in energy storage and conversion. Additionally, they provide flexibility in both physical, chemical and catalytic properties by substitution on the A- and B-site (Suntivich et al., 2011; Grimaud et al., 2013). A powerful descriptor for the catalytic activity is the d-band occupancy of the surface transition metal B-site, especially the occupancy of the anti-bonding states of the e_g-orbital, since it provides a stronger overlap with the oxygen-related adsorbate and directly promote electron transfer between surface cation and adsorbed reaction intermediates (Fujii and Zwart, 2011). Therefore, a variation of the oxidation state of the transition metal would lead to different catalytic activity in perovskite-type oxides. In the present work high-entropy ceramics with the formula $(Gd_{0.2}La_{0.2-x}Sr_xNd_{0.2}Sm_{0.2}Y_{0.2})(Co_{0.2}Cr_{0.2}Fe_{0.2}Mn_{0.2}Ni_{0.2})O_3$ ($x = 0$ and $x = 0.2$) are synthesized by mechanochemical synthesis (high-energy planetary ball milling) as well as a modified Pechini method. An in-depth comparison of the crystal structure, structural stability at high temperatures, microstructure and catalytic activity is carried out.

2 Experimental

2.1 Material preparation

Two different high-entropy perovskite-type materials (configurational entropy = 3.22 *R*) were synthesized and characterized, namely $(Gd,La,Nd,Sm,Y)_1(Co,Cr,Fe,Mn,Ni)_1O_3$ and $(Gd,Sr,Nd,Sm,Y)_1(Co,Cr,Fe,Mn,Ni)_1O_3$, hereafter referred to as high entropy oxide, HEO-La and HEO-Sr, respectively. Each of the two materials was prepared using two different synthesis routes: High-energy planetary ball milling and Pechini method. All chemicals were purchased from commercial sources (Alfa Aesar, ABCR GmbH, or Sigma Aldrich; purity ≥97%) and used without further purification.

2.1.1 High-energy planetary ball milling

For the synthesis of HEO-La, HEO-Sr, $LaCoO_3$, and $SrCoO_3$ the corresponding metal oxides (Gd_2O_3, Nd_2O_3, Sm_2O_3, Y_2O_3, La_2O_3, SrO, Co_3O_4, Cr_2O_3, Fe_2O_3, MnO_2, and NiO) were mixed and ball-milled for 24 h at 500 rpm under air using a high-energy planetary ball mill (Retsch PM 100, Retzsch GmbH). The weight ratio of ball to powder was 50:1. WC vials (50 ml volume) and WC balls (4 mm diameter) were used. All precursors were used directly without further pretreatment.

2.1.2 Pechini method

For the modified Pechini method, the respective nitrates (gadolinium nitrate hexahydrate, lanthanum nitrate hexahydrate, strontium nitrate, neodymium nitrate hexahydrate, samarium nitrate hexahydrate, yttrium nitrate hexahydrate, cobalt nitrate hexahydrate, chromium nitrate nonahydrate, iron nitrate nonahydrate, manganese nitrate tetrahydrate, and nickel nitrate hexahydrate) were first dissolved in 200 mL of demineralized water. Subsequently, citric acid (~19 g) and, after its dissolution, ~11 mL ethylene glycol was added at room temperature. The solution was heated to 100°C and kept at this temperature for about 2 h under constant stirring. Afterwards, the solution was heated to 300°C until a dried gel was obtained. The gel was ground and dried one more time at 350°C overnight. After repeated grinding, the material was finally calcined at 900 and 1,200°C for 12 h to obtain a fine powder.

2.2 Structural and microstructural characterization

2.2.1 Powder X-ray diffraction

XRD patterns were collected in the 2θ range of 10°–90° using a Bruker D8 diffractometer with Bragg-Brentano geometry and Cu-$K\alpha_{1,2}$ radiation source. Rietveld refinement was done by using TOPAS Academics V5 Software. The refinement was done with modifications to the elements and their proportion used in the

respective samples, based on the structure type $GdFeO_3$ (space groupe *Pbnm*). The instrumental intensity distribution was determined by employing a reference scan of SRM-1976b (strain-free Al_2O_3 in a glassy matrix with a particle size >2 μm).

2.2.2 Raman spectroscopy

Raman spectra were collected in the spectral region 100–1,000 cm^{-1} using an inVia confocal Raman microscope (RENISHAW). It should be noted that the infrared laser (λ = 785 nm, maximum laser power of 300 mW) and the green laser (λ = 532 nm, maximum laser power of 50 mW), which generally used to study the HEO, could not be used for these samples due to resonance effects. This could be due to presence of luminescent lanthanide ions and ultra-sensitivity of Raman to lanthanide luminescence (Yu et al., 2014). Hence, a He-Ne laser (λ = 633 nm, 50 mW) has been used for appropriate results. A grating with groove density of 1800 groves/mm (1,200 lines/mm) and a ×50 objective lens was used to collect the Raman spectra. The depth profiling of the samples was not possible, as the signal to noise ratio declined significantly. In order to avoid laser-irradiation-induced structural phase transition, accumulation time of 2 s, the laser power of ~1 mW (<10%) were used, while every spectrum recorded resulted from average of four acquisitions.

2.2.3 Scanning electron microscopy

SEM imaging was performed using a LEO-1530 electron microscope (Carl Zeiss AG).

2.2.4 Particle size distribution

Particle size analysis was performed by a Mastersizer 2000 laser scattering equipment. It consists in analyzing the dispersed light after focusing a laser onto a medium composed by the studied powder highly dispersed into ultra-pure water. The powders were initially dispersed into a small volume of ultra-pure water and sonicated for 10 min before analysis. The Mie Scattering theory method was used to treat the data and obtain the particle size distribution. As the refractive index and absorption of the material is required to run the model, the values were approximated by using the ones from Cr_2O_3 (RI = 2.5 and Absorption = 0.1).

2.2.5 Transmission electron microscopy

TEM and selected area electron diffraction (SAED) characterization were carried out with a probe corrected Themis-300 (Thermo Fisher Scientific) instrument operating at an accelerating voltage of 300 kV. The TEM specimen was prepared by dispersing the powder sample on a lacey carbon-coated TEM gold grid. The TEM is equipped with a Super-X energy dispersive X-ray spectroscopy (EDX) detector and a high-angle annular dark field scanning transmission electron microscopy (HAADF-STEM) detector, which are used to perform the HAADF-STEM imaging and EDX mapping, with a beam current of about 160 pA.

2.2.6 Inductively coupled plasma optical emission spectroscopy

The elemental concentration of the as-prepared samples was determined by inductively coupled plasma optical emission spectroscopy (ICP-OES). The samples were dissolved in aqua regia (HCl: HNO3, 3:1) and analyzed by performing a double determination using a ARCOS ICP-OES (Spectro Analytical Instruments, Kleve, Germany) with axial plasma view. Note that the oxygen fraction calculations assume that subtracting the cationic molar mass fractions determined by ICP-OES from the total molar mass yields the oxygen or anion mass fraction.

2.3 Electrochemistry

The electrocatalytic oxygen evolution reaction (OER) measurements were performed using a three-electrode setup on a modulated speed rotating rotator (Equilabrium SAS) equipped with a glassy carbon working electrode (Ø = 0.196 cm^2), Pt spiral counter electrode and Ag/AgCl reference electrode. The working electrode was prepared by dispersing, 10 mg of active material, 2 mg of carbon black (MTI Corporation), 100 μL Nafion binder (5 wt% Nafion in water/1-propanol, VWR International GmbH), in 100 μL ultra-pure water, produced and purified with a Millipore Milli-Q system (Merck KGaA), and 1800 μL 2-propanol (VWR, International GmbH, >99.9%) by an ultrasonic homogenizer (Scientz-IID, Ningbo Scientz Biotechnology Co.,) in an ice water bath for 30 min. For each measurement a total of 15 μL of the solution (an aliquot) was dropped on the working electrode (a catalyst loading of ~0.38 mg cm^{-2}) and dried at room temperature. OER performances were evaluated using a potentiostat (VSP, BioLogic GmbH) in O_2-saturated electrolyte of 1 M KOH (90%, reagent grade, Sigma Aldrich) at 25°C. All measurements were performed under constant O_2 gas flow. IrO_2 (AlfaAesar, Kandel, Germany, 99%) was used as reference material. An influence of the standard glassy carbon electrode on the electrochemical performance can be excluded (Mohanty et al., 2018; Dalai et al., 2019). Linear sweep voltammetry (LSV) curves were measured at a sweep rate of 10 mV s^{-1}. The Tafel slope was derived from LSV. The measured potentials vs. Ag/AgCl was converted to vs. reversible hydrogen electrode (RHE) by equation, $E_{RHE} = E_{Ag/AgCl} + 0.059\,pH + E^{\theta}_{Ag/AgCl\ vs\ RHE}$, where $E^{\theta}_{Ag/AgCl\ vs\ RHE}$ is 0.197 at 25 °C. The pH value of the electrolyte was measured by pH meter. The overpotential $\eta = E_{RHE}$—1.23.

3 Results and discussion

The aim of this research was to investigate the influence of different synthesis techniques on the material properties of high-entropy perovskite.

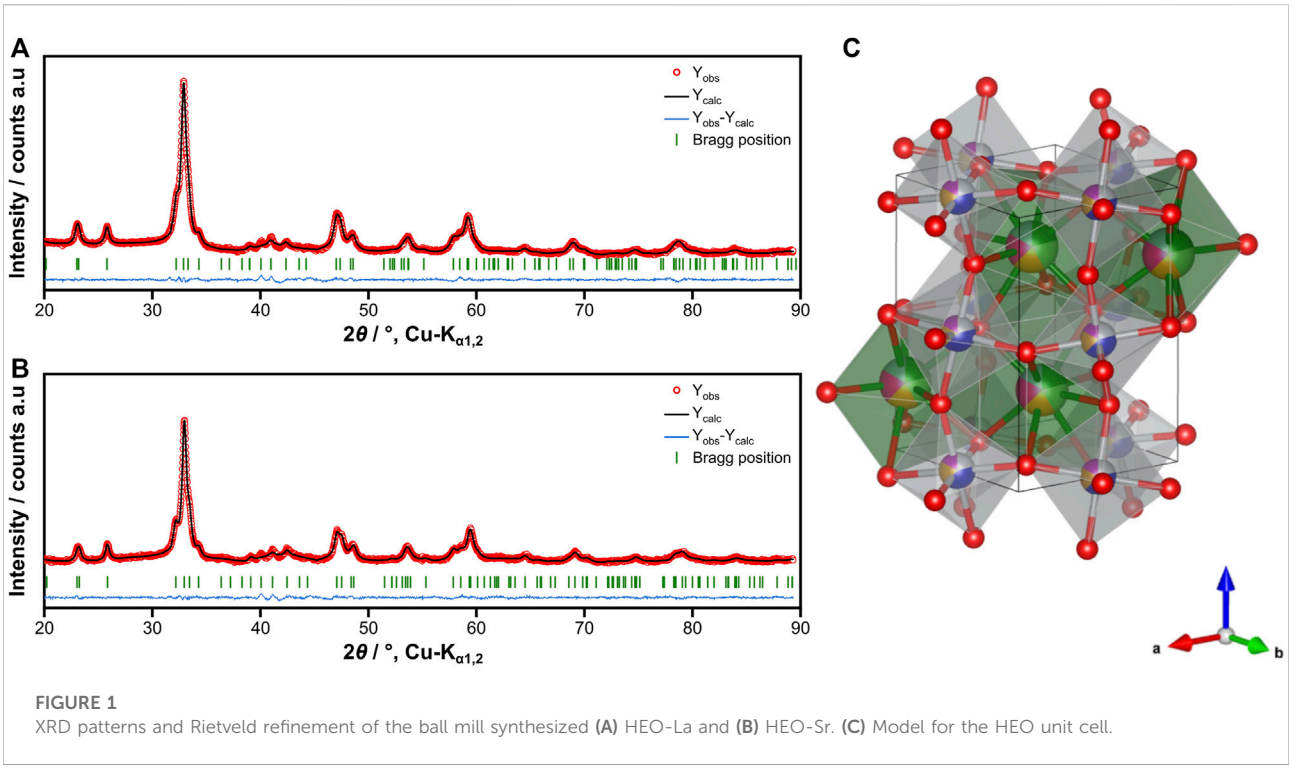

FIGURE 1
XRD patterns and Rietveld refinement of the ball mill synthesized **(A)** HEO-La and **(B)** HEO-Sr. **(C)** Model for the HEO unit cell.

For this purpose, two perovskite-type high-entropy materials $(Gd_{0.2}La_{0.2}Nd_{0.2}Sm_{0.2}Y_{0.2})$ $(Co_{0.2}Cr_{0.2}Fe_{0.2}Mn_{0.2}Ni_{0.2})O_3$ (HEO-La) and $(Gd_{0.2}Sr_{0.2}Nd_{0.2}Sm_{0.2}Y_{0.2})$ $(Co_{0.2}Cr_{0.2}Fe_{0.2}Mn_{0.2}Ni_{0.2})O_3$ (HEO-Sr) were synthesized using high-energy planetary ball milling and Pechini method. The perovskite-type materials prepared by ball milling are hereinafter referred to as HEO-La_BM and HEO-Sr_BM, and those prepared by the Pechini method as HEO-La_PM and HEO-Sr_PM. The crystal structure and phase purity of HEO-La and HEO-Sr were investigated using XRD and Rietveld refinement. The XRD diagrams for HEO-La and HEO-Sr show an orthorhombic crystal structure (space group: *Pbnm*) for both synthesis methods, ball milling and Pechini. Only for HEO-Sr, prepared using Pechini method, a secondary phase could be detected. The refinements for the ball milled HEO-La and HEO-Sr are shown in Figure 1. For the distribution and calculation of the occupancy of the metal A- and B-sites (ABO_3, A = Gd, Sr or La, Nd, Sm, and Y; B = Co, Cr, Fe, Mn, and Ni), it was assumed that the sites are completely and uniformly occupied by the metals (i.e., the sum is one). The B cations are each surrounded by six oxygen anions in the shape of octahedra, which form an edge-linked three-dimensional network. The gaps in this network contain the A cations, which have a coordination sphere of twelve oxygen anions in the form of a cuboctahedron as a coordination polyhedron. To examine possible tungsten carbide contamination from the high-energy planetary ball milling synthesis process, both materials were calcined after ball milling at 1,200°C to induce grain growth for better detection by X-ray diffraction. In both cases, no evidence of secondary phases could be identified, thereby excluding possible contamination or segregation (Supplementary Figure S1).

For both, HEO-La_BM and HEO-Sr_BM a relatively broad peak distribution was observed, indicating a nanostructured material, a result to be expected based on the synthesis route. Due to the exchange of lanthanum for strontium, slight changes in the lattice parameters of HEO-La_BM and HEO-Sr_BM were observed (Supplementary Table S1). Surprisingly, there was a decrease in the lattice parameters and consequently the unit cell volume ($V_{HEO\text{-}La\_BM}$ = 228.93 (5) Å^3; $V_{HEO\text{-}Sr\_BM}$ = 227.75 (6) Å^3) after the incorporation of strontium. This is remarkable, because the ionic radius of La^{3+} is smaller than that of Sr^{2+}, and the opposite trend was expected. Possibly, due to the exchange of La^{3+} for Sr^{2+}, charge compensation or even local changes in the oxide-framework are responsible for the decrease in lattice parameters. Nevertheless, since no other reflections were detected, it can be concluded that two phase-pure perovskite materials were successfully synthesized using high-energy planetary ball milling. Figure 2 shows SEM images at different magnifications of HEO-La_BM and HEO-Sr_BM. Agglomerates of different sizes were observed for both HEO-La_BM and HEO-Sr_BM. The agglomerates mostly consisted of a larger compact particle (about 5–40 µm) covered by nano-sized flake-like particles. In general, the particle size distribution is relatively inhomogeneous, which was confirmed by means of laser scattering shown in Supplementary Figure S2. The particle size distribution is between 0.5 and 100 µm. Even larger

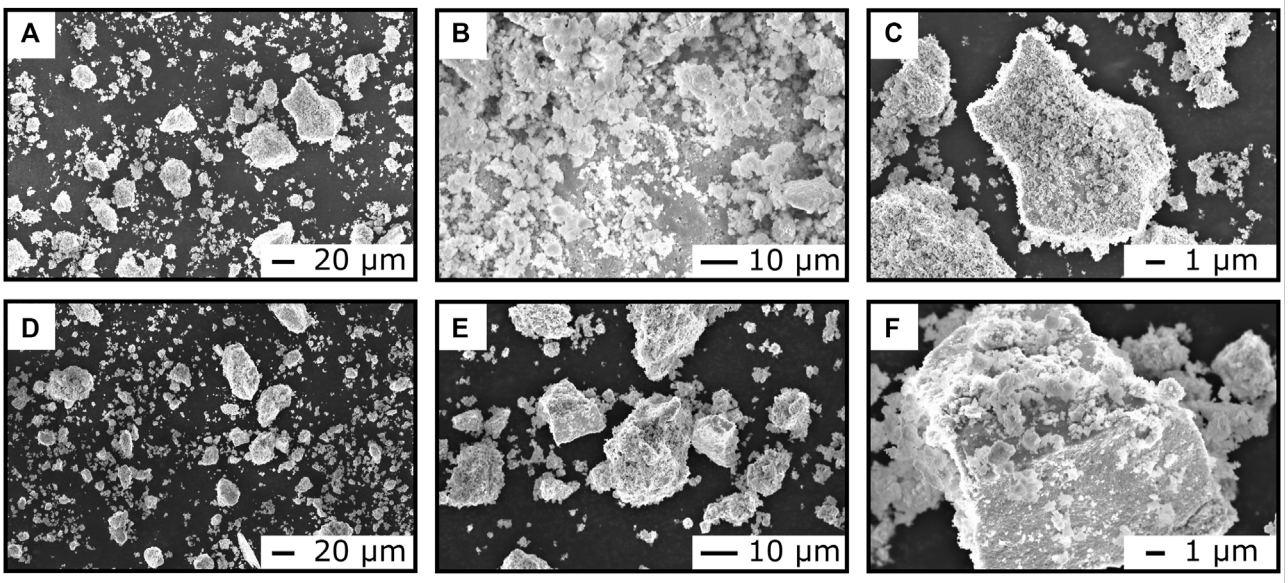

FIGURE 2
Top-view SEM images at different magnifications of HEO-La **(A–C)** and HEO-Sr **(D–F)** prepared by ball milling.

agglomerates were detected in HEO-La_BM, that might be due to measurement artifacts.

For a more homogeneous particle size distribution, both perovskite materials (HEO-La and HEO-Sr) were synthesized using the adapted Pechini method (see experimental section), as this achieves a uniform particle size (Dąbrowa et al., 2020). The XRD patterns and the corresponding Rietveld refinement for the perovskite-type HEOs prepared using Pechini method are shown in Figure 3. HEO-La_PM showed a phase-pure crystalline perovskite structure after both calcination temperatures (900°C and 1,200°C), while HEO-Sr_PM showed a secondary phase after both temperature treatments (see also TEM discussion). However, the amount of secondary phase was significantly reduced after increasing the calcination temperature from 900°C to 1,200°C. Therefore, only the materials calcined at 1,200°C will be considered in more detail in the following. The lattice parameters showed a similar behavior as already observed for the HEOs prepared by ball milling. Thus, an increase in lattice parameters was also observed after the exchange of La for Sr (Supplementary Table S1). Moreover, a decrease in the lattice parameters (*a*, *b*, *c*, and *V*) as well as better crystallinity was observed in both HEOs prepared using the Pechini method.

The perovskite materials HEO-La and HEO-Sr prepared by the Pechini method also exhibit agglomerates with different size distributions, like the materials prepared *via* ball milling technique (Figure 4). However, HEO-La_PM and HEO-Sr_PM did not show compact agglomerates, but a loose structure of individual point- or rod-shaped particles that were interconnected forming a network. The particle size distribution measured by means of laser scattering presented in Supplementary Figure S1 indeed showed a more uniform size distribution compared to the ball milled powders with particle sizes ranging from 1 to 100 µm. Although the mean particle size was not significantly altered by changing the synthesis method, but the powder morphology and size distribution were optimized. The uniform and smooth particle surface and narrower size distribution are expected to enhance reaction kinetics as well as processability and sinterability of the materials and thereby their integration into devises.

Raman spectroscopy measurements were performed on both HEO-La and HEO-Sr materials because transition metal oxides are known to be Raman active, and the spectra provide structural details on local molecular vibrations. As already mentioned ABO_3 perovskite structure consists of corner-linked B-cation octahedra with dodecahedral interstices of the A-cation (Chopelas, 2011). Based on the tilts and twists of the octahedra (according to the ratio of the cationic sizes), crystallization in different space groups is generally possible. With no tilts, twists, or distortions (centrosymmetric), the structure would have a cubic structure (*Pm3m*) and thus no Raman spectrum, i.e., A and B cations reside at inversion centres (Glazer, 1972). The HEO-La and HEO-Sr samples belong to orthorhombic perovskite structure with *Pbnm* symmetry which has four formula units per unit cell with the formula ABO_3. In both cases, HEO-La and HEO-Sr contain 0.2 mol of Sm^{3+}, Y^{3+}, Nd^{3+} and Gd^{3+} ions on the A site, along with either La^{3+} (HEO-La) or Sr^{2+} (HEO-Sr). The B-site cations are transition metal

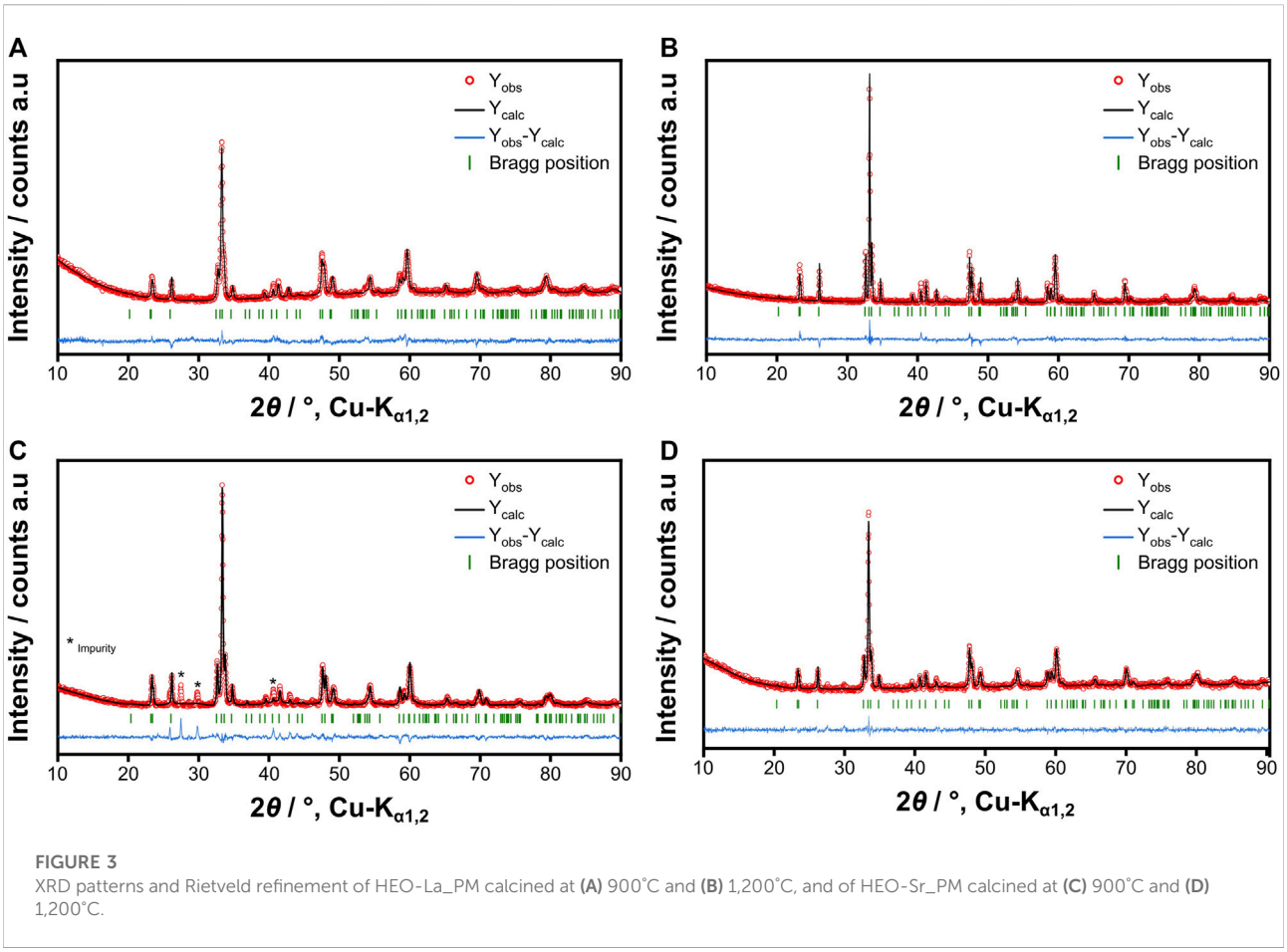

FIGURE 3
XRD patterns and Rietveld refinement of HEO-La_PM calcined at **(A)** 900°C and **(B)** 1,200°C, and of HEO-Sr_PM calcined at **(C)** 900°C and **(D)** 1,200°C.

elements, namely Ni, Co, Mn, Cr, and Fe, with the same composition for HEO-La and HEO-Sr samples. Accordingly, due to the presence of the different oxidation states of La (3^+) and Sr (2^+) on the A-site, either charge transfer reactions can occur to establish the charge neutrality (oxidation of the B-cations) or oxygen vacancies could be created. The group theory analysis suggests the presence of four first-order Raman-active modes such as A_{g+} B_{1g+} B_{2g+} B_{3g} (Selvarajan et al., 2019). As depicted in Figure 5, all HEO systems show distinct Raman bands at ~510 cm^{-1}, and ~627 cm^{-1} (Sarkar et al., 2020), which could be attributed to the bending (at 510 cm^{-1}, A_g vibrational mode) and stretching vibrations (627 cm^{-1}, B_g vibrational mode) of O–B–O groups (Dąbrowa et al., 2020). These values are comparable to the reports on $(La_{1-x}Sr_x)$ $(TM)O_{3-\delta}$ from Gupta and Whang (2007), Dąbrowa et al. (2020) and orthorhombic $LaMnO_3$ (Iliev et al., 1997).

The vibrational energies in Raman spectra depend on the effect of mass, valency, and size of the cations. The blue/red shifts in Raman bands are directly related to changes in the lattice volumes caused by different cations in the structure (Albedwawi et al., 2021). Substitution of the A cation implies that the framework structure remains unchanged while the volumes change slightly, affecting the degree of orthorhombic distortion (Chopelas, 2011). The distortion would result in bending, stretching or twisting of the bonds. The Raman modes attributed to oxygen motions would be similar, while the lowest energy modes would depend mainly on the mass of the A cation and would exhibit the change. However, in this case, no distinct bands at lower frequencies were observed. For ABO_3-type perovskite structures, Raman spectra versus composition revealed that, A cation plays the dominant role in determining the Raman shift (Chopelas, 2011). Comparing the A_g and B_g bands of HEO-La and HEO-Sr, a decrease in Raman shift is observed for the HEO-La samples. Band shifts are often associated with compositional changes that lead to expansion/contraction of the unit cells, variation in the M–O bond lengths and sometimes formation of oxygen defects (Reddy et al., 2007; Sarkar et al., 2017b). From Rietveld refinement, HEO-La samples show a slightly increased unit cell volume compared to HEO-Sr samples, which would lead to a decrease in Raman shift and would be a quite expected behaviour (Chopelas, 2011). Because the BO_6 clusters are also bonded to A cations, and vibrations of B-O bonds are therefore affected by the type of A cation involved, influencing the Raman shifts. This is confirmed by a positive shift

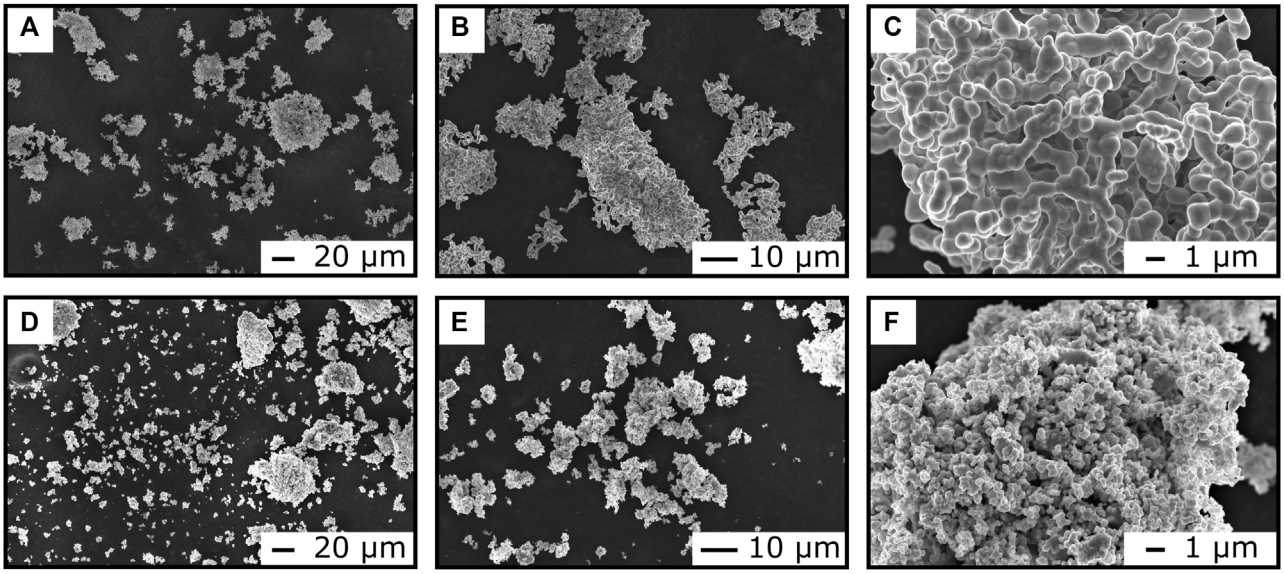

FIGURE 4
Top-view SEM images at different magnifications of HEO-La **(A–C)** and HEO-Sr **(D–F)** prepared using Pechini method. Both materials were calcined at 1,200°C and for 12 h.

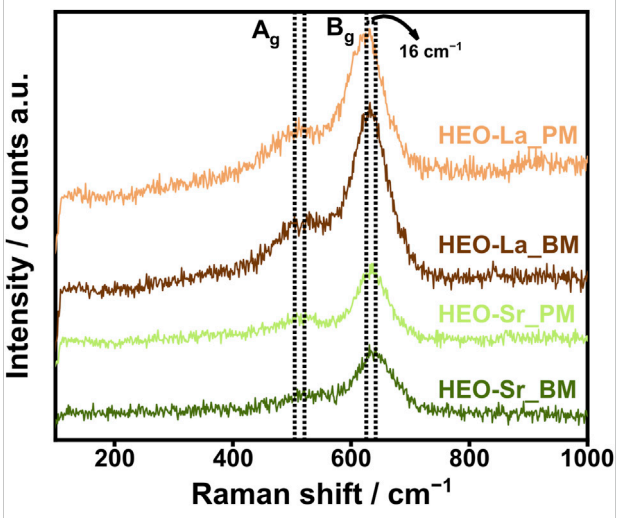

FIGURE 5
Raman spectra of HEO-La and HEO-Sr, synthesized using ball milling (BM) and Pechini method, obtained using a He–Ne laser (λ = 633 nm). The A_g vibration mode for O-B-O groups lies at ~ 510 cm^{-1}, whereas B_g band lies at ~ 622 cm^{-1}. HEO-La_PM and HEO-Sr_PM were calcined at 1,200°C for 12 h in air.

of A_g and B_g bands by 16 cm^{-1} in the case of HEO-Sr samples with lighter/larger Sr^{2+} ions. As the Sr^{2+} ions replace smaller La^{3+} ions, their presence hinders the amplitude of O-B-O vibrations and causes a decrease in the intensity of both bands. Furthermore, it appears that the synthesis method, has no significant effect on the Raman shifts, implying that the local structure and bond lengths are reproducible for both methods.

By comparing the integral intensities of the bands at 510 cm^{-1} and ~627 cm^{-1} (I_{Ag}/I_{Bg}), relative oxygen vacancy concentration could be approximated (Dąbrowa et al., 2020). The comparison of the individual intensity ratios indicate that the HEO-La and HEO-Sr samples have almost similar oxygen vacancy concentrations (I_{Ag}/I_{Bg} = 0.36 for HEO-La and 0.38 for HEO-Sr). This may be due to the low concentration of 0.2 mol of La^{3+} and Sr^{2+} substituted on the A-site, in their respective compositions, while keeping the framework structure constant with other A and B cations. Additionally, a change in oxidation state of the incorporated transition metals on the B-site is expected, and thereby a change in d-band occupancy, before oxygen vacancy formation. It is worth to note that, for a fair comparison of A_g/B_g intensity ratios, it is necessary to have an internal standard within the spectrum, i.e., intensity of peak, which is independent of substitutions/modifications. However, in this case, no such internal standard was available. Although this method does not provide quantitative information, it has been used as a reliable tool to approximate oxygen defects in different materials (Guo et al., 2011).

Based on the differences between HEO-La and HEO-Sr materials detected by XRD, SEM and Raman spectroscopy, the powder morphology and elemental distribution were investigated in more detail by transmission electron microscopy (TEM) and energy dispersive X-ray spectroscopy (EDX). Additionally, selected area electron diffraction (SAED)

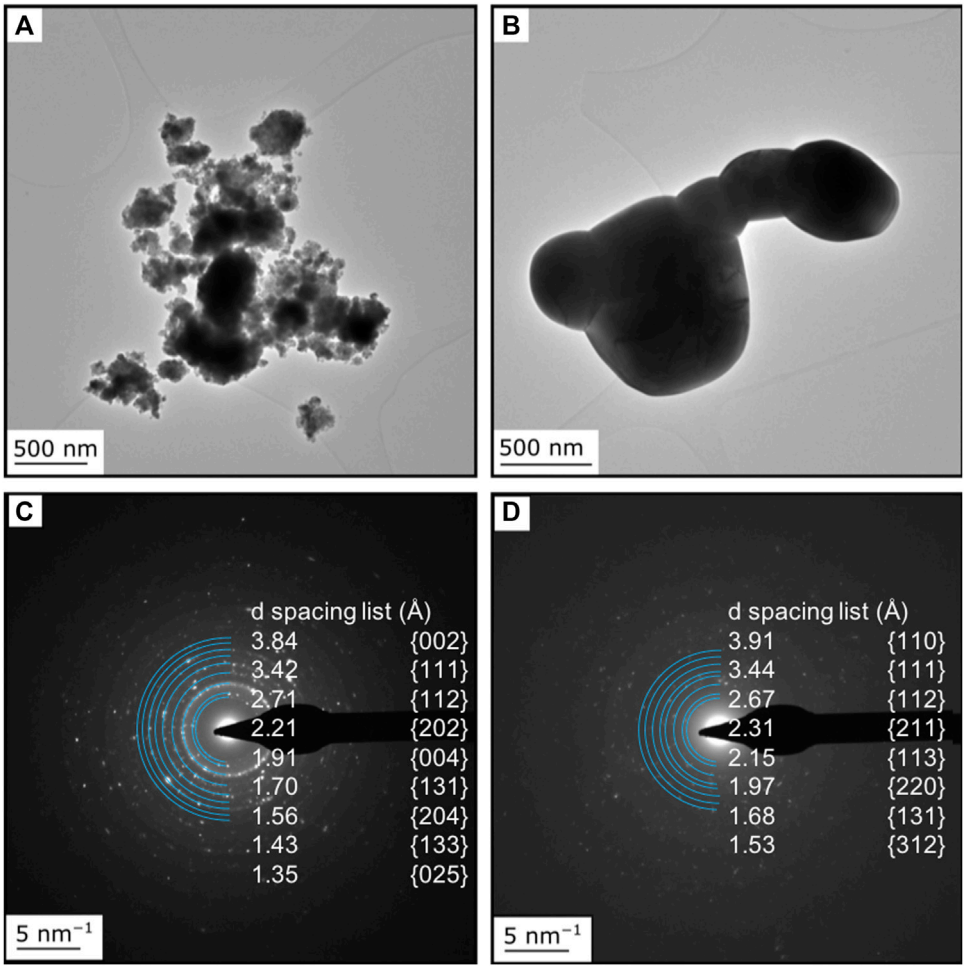

FIGURE 6
TEM images of **(A)** HEO-La_BM, **(B)** HEO-La_PM and SAED pattern for **(C)**HEO-La_BM and **(D)** HEO-La_PM with list of lattice spacings and corresponding hkl-planes of the Pbnm perovskite structure. HEO-La_PM and HEO-Sr_PM were calcined at 1,200°C for 12 h in air.

was performed to characterize the local crystal structure. Figure 6 shows the TEM and SAED results for HEO-La synthesized using both synthesis methods. Again, the powder morphology and particle surface show significant differences that would affect the processability of the powder. Additionally, the crystal structure for the ball milled powder was easily identified as a *Pbnm* perovskite-type structure, while the diffraction pattern for the powder synthesized using the Pechini method was not clear. This is because the particle size distribution of the powder prepared by the ball mill sometimes contains very small particles suitable for SAED. While this was not the case for the samples prepared by the Pechini method.

The same can be observed for the HEO-Sr materials (Figure 7). A single-phase orthorhombic perovskite structure was identified for the ball milled sample, while additional secondary phases cannot be excluded for the Pechini method synthesized sample, which agrees with XRD results.

HAADF images and EDX analysis for HEO-Sr is presented in Figure 8. Most elements are homogenously distributed across the imaging area. The only exception is observed for Sr and Cr in the Pechini synthesized powder (Figure 8A). Since the segregation of these two elements is located on the same particle it is assumed that the observed secondary phase is a compound with larger Cr- and Sr-content. The ball milled powder shows a homogeneous elemental distribution for the HEO-Sr material (Figure 8B), while a small Co segregation is present for HEO-La_BM shown in Supplementary Figure S3. HEO-La_PM shown in Supplementary Figure S4 exhibits homogeneous elemental distribution. All small elemental segregations are localized at individual particles and do not show any increased concentration at particle surfaces. Therefore, it is evident that for all materials the particle surfaces, that are crucial for any redox activity, have a homogeneous elemental distribution for A- and B-site cations as well as oxygen. This allows for a direct comparison of the

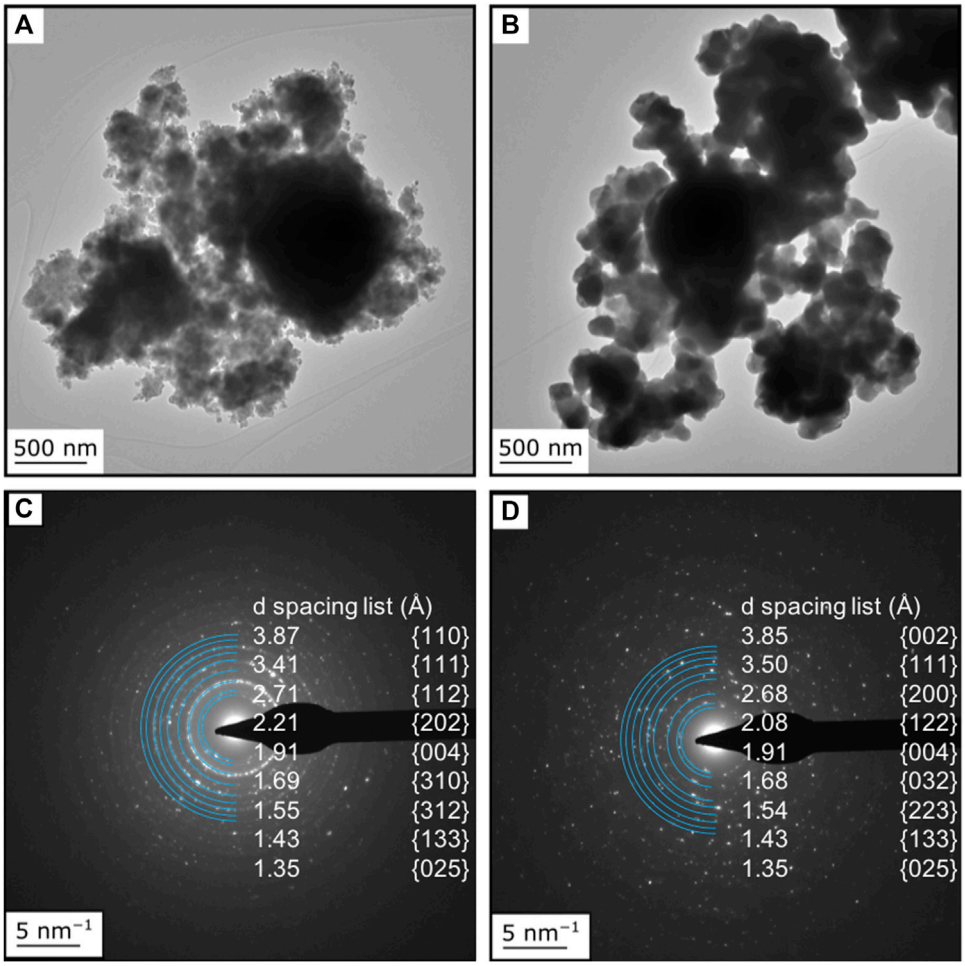

FIGURE 7
TEM images of **(A)** HEO-Sr_BM, **(B)** HEO-Sr_PM and SAED pattern for **(C)** HEO-Sr_BM and **(D)** HEO-Sr_PM with list of lattice spacings and corresponding hkl-planes of the Pbnm perovskite structure. HEO-La_PM and HEO-Sr_PM were calcined at 1,200°C for 12 h in air.

catalytic activity of all materials. The EDX sprectra are presented in Supplementary Figure S5. Additionally, ICP-OES results (Supplementary Tables S2, S3) show a good agreement with nominal cation content for both materials synthesized using the Pechini method, while ball milled samples show a sub-stochiometric content of Nd and Cr. This might be due to water adsorption on the oxide precursors. Nevertheless, this minor difference is not expected to have a significant influence on material properties. The oxygen stoichiometry (n_O) calculated according to the total cationic weight percentage of both material compositions synthesized using Pechini method and ball milling is $n_O = 2.8$ and $n_O = 3$ mol per formula unit, respectively. This indicates that the La^{3+} substitution by Sr^{2+} does not alter oxygen vacancy concentration in the materials, and a change of B-site oxidation state is rather expected. The near stochiometric oxygen content for the ball milled samples and its stability after La substitution is in good agreement with the results obtained from Raman. On the other hand, samples prepared using the Pechini method display a sub-stoichiometric oxygen content, which might lead to enhanced catalytic activity through the introduction of oxygen vacancies during synthesis, presence of a minute impurity phase with lower oxygen stoichiometry or even metal alloying.

The catalytic performance of HEO-La_BM, HEO-La_PM, HEO-Sr_BM and HEO-Sr_PM for the OER was tested in an alkaline medium. (see experimental section) Initial CV steps before OER are performed to activate the material. As can be seen in Figure 9, there are significant differences in OER performance between the two materials (HEO-La and HEO-Sr). Furthermore, the synthesis route does not seem to have an influence on OER performance. For example, an overvoltage of 360 and 370 mV at 10 mA/cm^2 was observed for HEO-Sr_PM and HEO-Sr_BM, respectively. Even with increasing current density, no significant

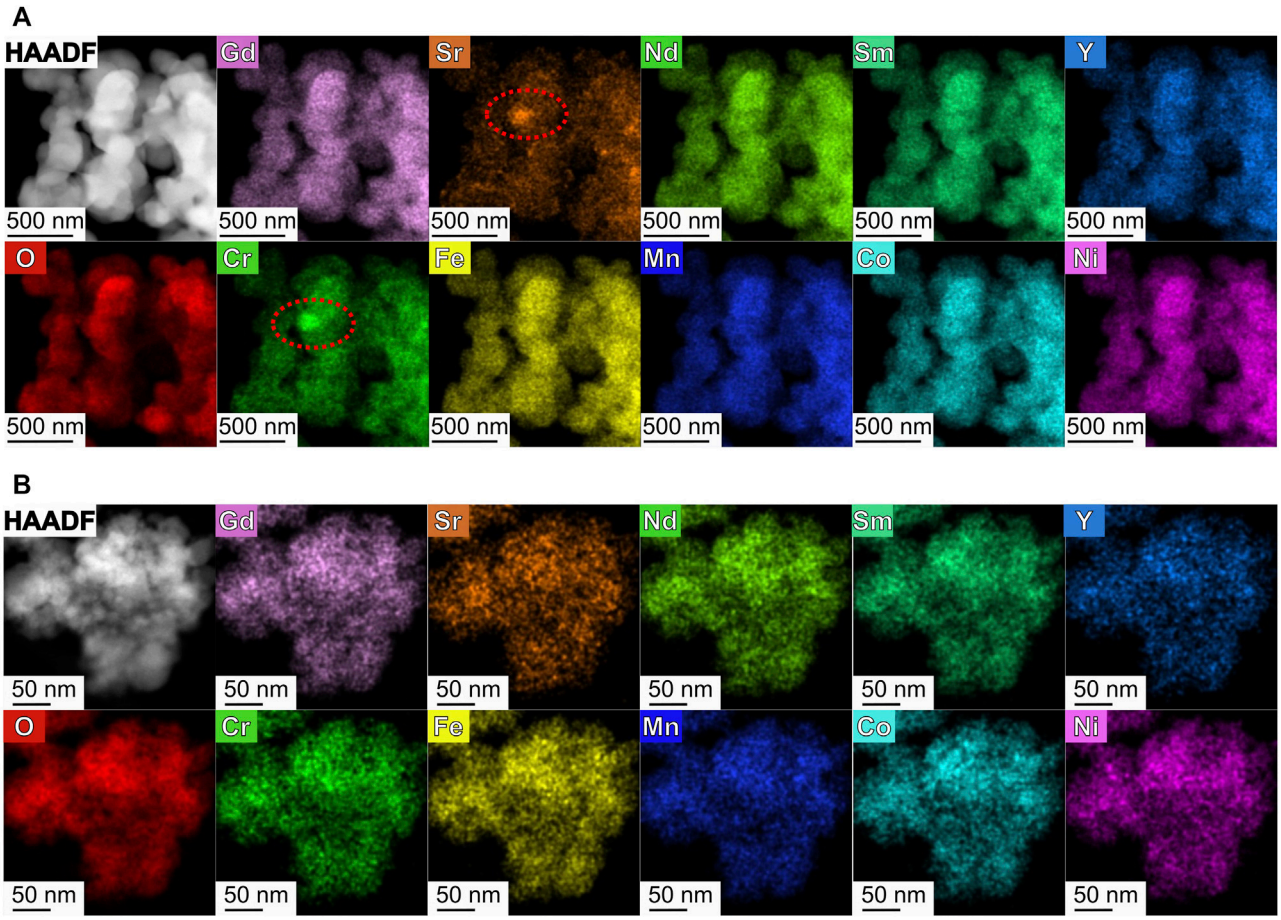

FIGURE 8
HAADF images and EDX analysis **(A)** HEO-Sr_PM and **(B)** HEO-Sr_BM. Elemental segregations in HEO-Sr_PM are highlighted by red dashed circle. HEO-Sr_PM were calcined at 1,200°C for 12 h in air.

difference was observed between HEO-Sr_BM and HEO-Sr_PM. The change in composition seems to have a strong influence on the catalytic activity. HEO-La_BM and HEO-La_PM show an overvoltage of 400 and 450 mV, respectively, at 10 mA/cm^2. With increasing potential, no more current/current density could be detected. Since the LSV measurement is a voltametric measurement in which the current at the working electrode is measured while the potential between the working electrode and the reference electrode increases linearly in time, this shows that the HEO-La materials exhibit significantly lower activity. To get further insights into the OER kinetics, Tafel plots of the different electrocatalysts were extracted from the LSV curves (Figure 9C) with values of 63 and 48 mA dec^{-1} for HEO-Sr_BM and HEO-Sr_PM, respectively, whereas HEO-La_BM and HEO-La_PM exhibited much lower kinetics with approximately 70 mA dec^{-1}. Since the OER is a morphology-dependent catalytic reaction, the electrochemical surface area (ECSA) was determined by the double layer capacitance (C_{dl}) estimated by cyclic voltammetry (CV) measurements in a non-faradaic region (Supplementary Figure S6). The C_{dl} values of HEO-La_BM, HEO-La_PM, HEO-Sr_BM, and HEO-Sr_PM are 1.47, 0.59, 4.37, und 0.71 mF cm^{-2}; and the ECSA values are 36.75, 14.75, 109.25, and 17.75 cm^2 respectively. The LSV curves were then normalized to the ECSA to evaluate the intrinsic activity (Supplementary Figure S7). HEO-Sr_PM shows the highest intrinsic catalytic activity. Generally, it can be observed that the materials produced by the Pechini method have a significantly enhanced intrinsic catalytic activity. Additionally, the significantly improved catalytic activity of the strontium-containing perovskite-type materials (HEO-Sr_BM and HEO-Sr_PM, Figure 9) can probably be attributed to the change in the oxidation states on the B-site due to the exchange of La^{3+} for Sr^{2+}. A comparable behavior has already been observed in Sr substitution studies on e.g. $La_{1-x}Sr_xNiO_3$, $La_{1-x}Sr_xCoO_3$, $La_{1-x}Sr_xFe_{1-y}Co_yO_3$ (Matsumoto et al., 1980; Cheng et al., 2015; Mefford et al., 2016). Based on DFT calculations, the

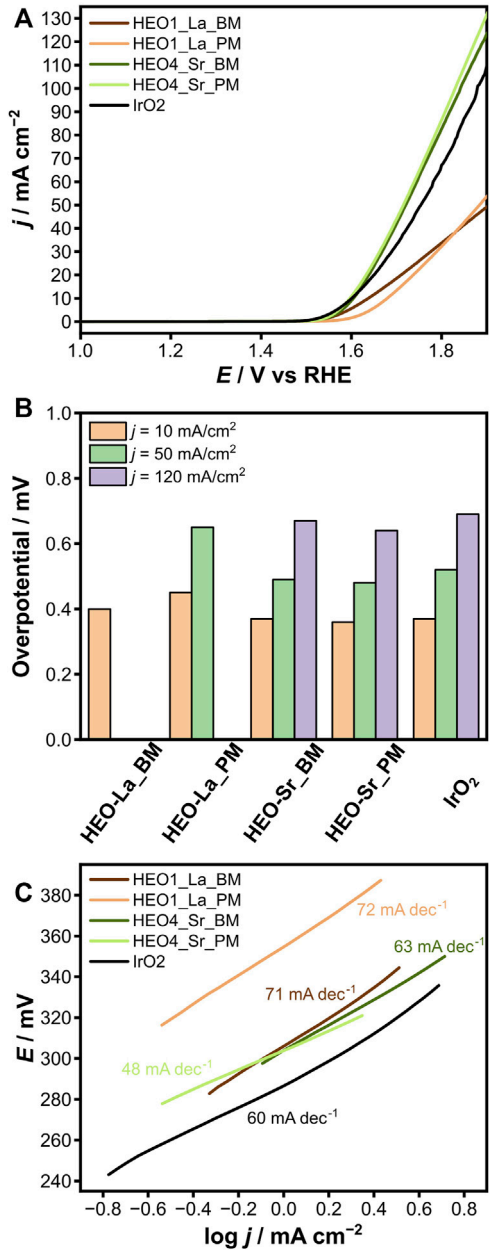

FIGURE 9
OER performance for HEO-La and HEO-Sr prepared using both ball milling (BM) and Pechini method (PM) **(A)** linear potential sweep voltammogram, **(B)** comparison of overpotential, **(C)** Tafel plot with the slope indicated. HEO-La_PM and HEO-Sr_PM were calcined at 1,200°C for 12 h in air.

improved electrochemical OER activity can be attributed to the incorporation of Sr, leading to a straightening of the octahedral cage and an alignment of the atoms along the B-O-B bond. Furthermore, the oxidation of the B cations enhances the overlap between the occupied O 2p valence bands and the occupied B-cation 3d conduction bands, which generally explains an improvement in the electronic conductivity as a function of Sr content (Mefford et al., 2016). Therefore, it can be assumed that these are the main reasons for the improved OER activity of the HEO-Sr samples. Moreover, the catalytic activities of HEO-Sr samples are comparable or even slightly better than the activities of the state-of-the-art material IrO_2 used for OER reactions ($\eta_{10\,mA/cm^2}$ = 370 mV and Tafel slope = 60 mA dec^{-1}).

We would like to point out that even if we cannot make a clear statement about oxygen vacancies, vacancies are still a possible reason for the better OER performance of HEO-Sr materials, because the incorporation of strontium leads either to a change in oxidation states on the B-site or to oxygen vacancy formation, latter being directly correlated to the change in OER. The specific generation of oxygen vacancies by doping or varying the material composition in order to improve the OER performance or the electrochemical catalytic activity in general is an approach that has already been extensively investigated and should not be over seen (Badreldin et al., 2020; Zhu et al., 2020; Mir and Pandey, 2021).

In addition, the OER performance of the high-entropy materials was compared with the performance of low-entropy materials. For this purpose, $LaCoO_3$ and $SrCoO_3$ synthesized using the Pechini method were used as comparison (Supplementary Figure S8). Both materials show lower performance compared to the HEMs and IrO_2 (η_{LaCoO_3} = 470 mV and η_{SrCoO_3} = 480 mV at 10 mA/cm²). This shows that the high-entropy concept and the associated tailoring of material properties is a promising approach for the preparation of new improved OER catalysts. Therefore, it would be of great interest to study how a further increase of Sr or a mixing of La and Sr content could affect the OER activity for the perovskite-type high-entropy materials. Furthermore, future studies on compositional optimization and exchange of B-site cations and determination of their influence on OER activity, will be of significant interest.

4 Conclusion

This work presents the synthesis of novel high-entropy perovskite-type materials by means of two different synthesis methods, high-energy planetary ball milling and a modified Pechini method. While ball milling leads to a pure perovskite phase, the powder morphology is not optimal for further processing and sintering, hindering the material integration into electrochemical devices. The Pechini method, on the other hand, delivers a uniform particle size distribution and thus better powder processability. The elemental distribution along the particle surfaces is homogeneous for HEO-La and HEO-Sr irrespective of the synthesis method. The La^{3+} substitution by Sr^{2+} did not necessarily lead to oxygen vacancy formation according to findings from Raman and ICP-OES but the charge compensation is more likely by change in oxidation

state of the various B-site cations. Resulting catalytic activity of HEO-Sr is by far superior to the La containing counterpart and even slightly exceeds the performance of the state-of-the-art IrO_2 catalyst. An enhanced intrinsic catalytic activity was observed for the materials synthesized using the Pechini method. Additionally, a comparison to the single element counterparts confirms the promising potential of high-entropy materials for energy applications and the advantage they offer to design novel materials at lower environmental impact and cost, while achieving enhanced properties compared to conventional materials.

Data availability statement

The original contributions presented in the study are included in the article/Supplementary Material, further inquiries can be directed to the corresponding authors.

Author contributions

SS and LL optimized and prepared the samples by different methods. AA helped while optimizing the Pechini method. SS also performed X-ray diffraction and its refinement, SEM and catalysis experiments. YT performed TEM and all related measurements (EDX, SAED). GK performed Raman measurements and contributed to the manuscript preparation. LB performed light scattering measurements. BB provided essential lab equipment and expertise in high-entropy material design. MF, AT, and HH provided guidance and fruitful discussions. SS and MB layed the basic concept of the study and organized the working procedures to achieve high-quality research and jointly wrote the manuscript.

Acknowledgments

The authors acknowledge the support from EPISTORE project funded by the European Union's Horizon 2020 research and innovation program under grant agreement No. 101017709. This research was partially funded by the Generalitat de Catalunya (2017 SGR 1421, NANOEN). MB and AA acknowledge the support of the German Research Foundation (DFG) projects No. SE 1407/4-2 and No. 424789449, respectively. LL acknowledge financial support from the China Scholarship Council (CSC). YT, GK, and MF acknowledge the financial support from German Research Foundation (DFG) under Project ID 390874152 (POLiS Cluster of Excellence, EXC 2154). This work contributes to the research performed at CELEST (Center for Electrochemical Energy Storage Ulm-Karlsruhe). The authors would like to thank Karlsruhe Nano Mikro Facility (KNMF) for the access to transmission microscopy equipment and data analysis. We acknowledge support by the KIT-Publication Fund of the Karlsruhe Institute of Technology.

Conflict of interest

The authors declare that the research was conducted in the absence of any commercial or financial relationships that could be construed as a potential conflict of interest.

Publisher's note

All claims expressed in this article are solely those of the authors and do not necessarily represent those of their affiliated organizations, or those of the publisher, the editors and the reviewers. Any product that may be evaluated in this article, or claim that may be made by its manufacturer, is not guaranteed or endorsed by the publisher.

Supplementary material

The Supplementary Material for this article can be found online at: https://www.frontiersin.org/articles/10.3389/fenrg.2022.983979/full#supplementary-material

References

Albedwawi, S. H., AlJaberi, A., Haidemenopoulos, G. N., and Polychronopoulou, K. (2021). High entropy oxides-exploring a paradigm of promising catalysts: A review. *Mat. Des.* 202, 109534. doi:10.1016/j.matdes.2021.109534

Badreldin, A., Abusrafa, A. E., and Abdel-Wahab, A. (2020). Oxygen-deficient perovskites for oxygen evolution reaction in alkaline media: A review. *emergent Mat.* 3, 567–590. doi:10.1007/s42247-020-00123-z

Cheng, X., Fabbri, E., Nachtegaal, M., Castelli, I. E., El Kazzi, M., Haumont, R., et al. (2015). Oxygen evolution reaction on La1−xSrxCoO_3 perovskites: A combined experimental and theoretical study of their structural, electronic, and electrochemical properties. *Chem. Mat.* 27, 7662–7672. doi:10.1021/acs.chemmater.5b03138

Chopelas, A. (2011). Single-crystal Raman spectra of YAlO3 and GdAlO3: Comparison to several orthorhombic ABO3 perovskites. *Phys. Chem. Min.* 38, 709–726. doi:10.1007/s00269-011-0444-1

Dąbrowa, J., Olszewska, A., Falkenstein, A., Schwab, C., Szymczak, M., Zajusz, M., et al. (2020). An innovative approach to design SOFC air electrode materials: High entropy $La_{1-x}Sr_x$(Co, Cr, Fe, Mn, Ni)$O_{3-\delta}$(x= 0, 0.1, 0.2, 0.3) perovskites synthesized by the sol–gel method. *J. Mat. Chem. A* 8, 24455–24468. doi:10.1039/d0ta06356h

Dalai, N., Mohanty, B., Mitra, A., and Jena, B. (2019). Highly active ternary nickel–iron oxide as bifunctional catalyst for electrochemical water splitting. *ChemistrySelect* 4, 7791–7796. doi:10.1002/slct.201901465

Fujii, M. S., and Zwart, S. P. (2011). The origin of OB runaway stars. *Science* 334, 1380–1383. doi:10.1126/science.1211927

Glazer, A. M. (1972). The classification of tilted octahedra in perovskites. *Acta Crystallogr. Sect. B* 28, 3384–3392. doi:10.1107/s0567740872007976

Grimaud, A., May, K. J., Carlton, C. E., Lee, Y. L., Risch, M., Hong, W. T., et al. (2013). Double perovskites as a family of highly active catalysts for oxygen evolution in alkaline solution. *Nat. Commun.* 4, 2439. doi:10.1038/ncomms3439

Guo, J., Sun, A., Chen, X., Wang, C., and Manivannan, A. (2011). Cyclability study of silicon–carbon composite anodes for lithium-ion batteries using electrochemical impedance spectroscopy. *Electrochim. Acta* 56, 3981–3987. doi:10.1016/j.electacta.2011.02.014

Gupta, R. K., and Whang, C. M. (2007). Structural study of a sol–gel derived novel solid oxide fuel cell perovskite: (La1−xSrx)($Cr_{0.85}Fe_{0.05}Co_{0.05}Ni_{0.05}$)$O_{3-\delta}$. *J. Phys. Condens. Matter* 19, 196209. doi:10.1088/0953-8984/19/19/196209

Iliev, M., Lee, H., Popov, V., Abrashev, M. V., Hamed, A., Meng, R. L., et al. (1997). Raman- and infrared-active phonons in hexagonalYMnO3: Experiment and lattice-dynamical calculations. *Phys. Rev. B* 56, 2488–2494. doi:10.1103/physrevb.56.2488

Lin, L., Wang, K., Azmi, R., Wang, J., Sarkar, A., Botros, M., et al. (2020). Mechanochemical synthesis: Route to novel rock-salt-structured high-entropy oxides and oxyfluorides. *J. Mat. Sci.* 55, 16879–16889. doi:10.1007/s10853-020-05183-4

Ma, Y., Ma, Y., Wang, Q., Schweidler, S., Botros, M., Fu, T., et al. (2021). High-entropy energy materials: Challenges and new opportunities. *Energy Environ. Sci.* 2021, 2883–2905. doi:10.1039/d1ee00505g

Matsumoto, Y., Yamada, S., Nishida, T., and Sato, E. (1980). Oxygen Evolution on La1 – x Sr x Fe1 – y Co y O 3 Series Oxides. *J. Electrochem. Soc.* 127, 2360–2364. doi:10.1149/1.2129415

Mefford, J. T., Rong, X., Abakumov, A. M., Hardin, W. G., Dai, S., Kolpak, A. M., et al. (2016). Water electrolysis on La1−xSrxCoO3−δ perovskite electrocatalysts. *Nat. Commun.* 7, 11053. doi:10.1038/ncomms11053

Mir, R. A., and Pandey, O. P. (2021). Role of morphological features and oxygen vacancies on electrocatalytic oxygen evolution reaction (OER) activity and pseudocapacitance performance of $BiVO_4$ structures. *Appl. Phys. Lett.* 118, 253902. doi:10.1063/5.0057082

Mohanty, B., Ghorbani-Asl, M., Kretschmer, S., Ghosh, A., Guha, P., Panda, S. K., et al. (2018). MoS_2 quantum dots as efficient catalyst materials for the oxygen evolution reaction. *ACS Catal.* 8, 1683–1689. doi:10.1021/acscatal.7b03180

Reddy, B. M., Bharali, P., Saikia, P., Khan, A., Loridant, S., Muhler, M., et al. (2007). Hafnium doped ceria nanocomposite oxide as a novel redox additive for three-way catalysts. *J. Phys. Chem. C* 111, 1878–1881. doi:10.1021/jp068531i

Rost, C. M., Sachet, E., Borman, T., Moballegh, A., Dickey, E. C., Hou, D., et al. (2015). Entropy-stabilized oxides. *Nat. Commun.* 6, 8485. doi:10.1038/ncomms9485

Sarkar, A., Djenadic, R., Usharani, N. J., Sanghvi, K. P., Chakravadhanula, V. S. K., Gandhi, A. S., et al. (2017). Nanocrystalline multicomponent entropy stabilised transition metal oxides. *J. Eur. Ceram. Soc.* 37, 747–754. doi:10.1016/j.jeurceramsoc.2016.09.018

Sarkar, A., Eggert, B., Velasco, L., Mu, X., Lill, J., Ollefs, K., et al. (2020). Role of intermediate 4*f* states in tuning the band structure of high entropy oxides. *Apl. Mat.* 8, 051111. doi:10.1063/5.0007944

Sarkar, A., Loho, C., Velasco, L., Thomas, T., Bhattacharya, S. S., Hahn, H., et al. (2017). Multicomponent equiatomic rare Earth oxides with a narrow band gap and associated praseodymium multivalency. *Dalton Trans.* 46, 12167–12176. doi:10.1039/c7dt02077e

Selvarajan, P., Chandra, G. K., Bhattacharya, S., Sil, S., Vinu, A., and Umapathy, S. (2019). Potential of Raman spectroscopy towards understanding structures of carbon-based materials and perovskites. *emergent Mat.* 2, 417–439. doi:10.1007/s42247-019-00052-6

Suntivich, J., May, K. J., Gasteiger, H. A., Goodenough, J. B., and Shao-Horn, Y. (2011). A perovskite oxide optimized for oxygen evolution catalysis from molecular orbital principles. *Science* 334, 1383–1385. doi:10.1126/science.1212858

Wang, J., Stenzel, D., Azmi, R., Najib, S., Wang, K., Jeong, J., et al. (2020). Spinel to rock-salt transformation in high entropy oxides with Li incorporation. *Electrochem* 1, 60–74. doi:10.3390/electrochem1010007

Wang, Q., Sarkar, A., Li, Z., Lu, Y., Velasco, L., Bhattacharya, S. S., et al. (2019). High entropy oxides as anode material for Li-ion battery applications: A practical approach. *Electrochem. Commun.* 100, 121–125. doi:10.1016/j.elecom.2019.02.001

Yu, J., Cui, L., He, H., Yan, S., Hu, Y., and Wu, H. (2014). Raman spectra of RE2O3 (RE=Eu, Gd, Dy, Ho, Er, Tm, Yb, Lu, Sc and Y): Laser-excited luminescence and trace impurity analysis. *J. Rare Earths* 32, 1–4. doi:10.1016/s1002-0721(14)60025-9

Zhu, K., Shi, F., Zhu, X., and Yang, W. (2020). The roles of oxygen vacancies in electrocatalytic oxygen evolution reaction. *Nano Energy* 73, 104761. doi:10.1016/j.nanoen.2020.104761